Journal of Structural Biology 198 (2017) 116–123

Contents lists available at ScienceDirect

Journal of Structural Biology

journal homepage: www.elsevier.com/locate/yjsbi

The structure of the "amorphous" matrix of keratins

Murat Kadir [a], Xinwei Wang [b], Bowen Zhu [b], Jing Liu [b], Duane Harland [c], Crisan Popescu [d,*]

[a] Lubrizol Advanced Materials, Inc., 9911 Brecksville Road, Brecksville, OH 44141, USA
[b] Department of Mechanical Engineering, 2025 Black Engineering Building, Iowa State University, Ames, IA 50011, USA
[c] AgResearch Limited, Lincoln Research Centre, Private Bag 4749, Christchurch 8140, New Zealand
[d] KAO Germany GmbH, Pfungstädterstr. 98-100, D-64297 Darmstadt, Germany

ARTICLE INFO

Article history:
Received 12 November 2016
Received in revised form 31 March 2017
Accepted 1 April 2017
Available online 5 April 2017

Keywords:
Keratin
Matrix
Phonon
Spin-diffusion
Transmission electron microscopy

ABSTRACT

Various keratin fibers, particularly human hairs, were investigated by transmission electron microscopy, TEM, solid-state ^{1}H NMR and Transient Electro-Thermal Technique, TET. The results converge to suggest that the matrix of keratin fiber cortex, far from being amorphous, has a well-defined nano-scale grainy structure, the size of these grains being around 2–4 nm. The size of the grains appears to strongly depend on the chemical treatment of the fiber, on the temperature and on the relative humidity of the environment, as well as on the physiological factors at the level of fiber production in follicle.

By suggesting an organization at the nano-scale of the protein chains in these grains, likely to be Keratin Associated Proteins, the results challenge the view of matrix as a homogeneous glassy material. Moreover, they indicate the potential of further investigating the purpose of this structure that appears to reflect not only chemical treatments of keratins but also biological processes at the level of the follicle.

1. Introduction

Trichokeratins are a key protein constituent of the mammalian solution to the need for hard, lightweight and chemically resistant structures, e.g., hairs, claws, hooves and horns (Wang et al., 2016; Popescu and Hoecker, 2007). Different from other fibrous proteins (Schrooyen et al., 2000), such as collagen, elastin and myofibrillar proteins, trichokeratin (or hard keratin) normally provides outer covering and protection of organisms due to the large amount of disulfide bonds (Trabbic and Yager, 1998) and a unique three-dimensional structure (Zhao et al., 2003; Lynch et al., 1986).

Hard keratin structures, wool and human hair in particular, have been historically well studied for industrial reasons. The *meso*-structure of the fibril-matrix composite as established using X-ray and electron-based methods is summarized in Fig. 1.

In a very simplistic way one may depict keratin materials as being composed of keratin intermediate filaments, KIF, surrounded by the matrix (dark area between KIFs in Fig. 1). A more detailed description takes into account also the existence of an interface between KIFs and surrounding matrix, formed of heads and tails of the filaments protruding and connecting into matrix, as well as of other ionic and covalent bonds between side aminoacids of filaments and surrounding matrix (Istrate et al., 2013). While the KIFs are known from a bulk of experimental data to be well organized, crystalline structures (Fraser et al., 1964), the matrix is largely assumed as an amorphous material gluing the filaments and the interface phase is considered as being a very thin layer of the size of a bond length.

The present work aims at challenging the view of matrix as a homogeneous glassy material by investigating its nano-structure for accessing details which may reveal protein organization at that scale. It also looks at how various chemical treatments affect this organization.

2. Experimental

2.1. TEM

For transmission electron microscopy, New Zealand Romney mid-side wool fibers were scoured with detergent (Teric GN9) and then heptane, air dried and mounted across an acetate frame as in earlier studies (Harland et al., 2011b). Quills from African crested porcupine (*Hystrix cristata*) were also chosen based on observations that compared to other quills those from *H. cristata* have a particularly regular internal structure in X-ray diffraction experiments (Parry and Fraser, 2015). Individual quills were washed in water and cut into small transverse or longitudinal strips, avoiding the medulla. Strips were mounted on acetate

* Corresponding author.
E-mail addresses: murat.kadir@lubrizol.com (M. Kadir), xwang3@iastate.edu (X. Wang), duane.harland@agresearch.co.nz (D. Harland), crisan.popescu@kao.com (C. Popescu).

http://dx.doi.org/10.1016/j.jsb.2017.04.001
1047-8477/

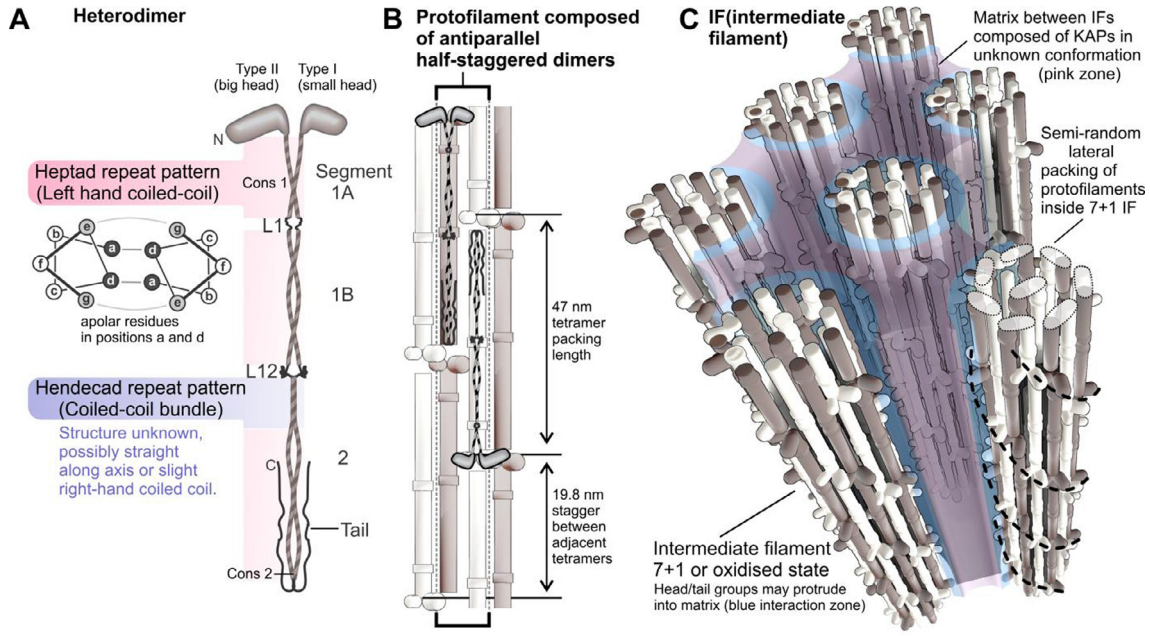

Fig. 1. Keratin fiber structure as it is currently understood. **A**. Heterodimers of Type I and Type II keratin are held in a rod-like conformation by heptad and hendecad coiled-coil segments interrupted by two flexible linkers (Smith et al., 2002; Parry, 2006; Chernyatina et al., 2015). Head and tail segments contain only local regions of structural regularity, but likely play a part in stable filament assembly. **B**. Dimers within a filament form tetramers composed of antiparallel dimers which stack longitudinally, we assume here an A11 or A22 oxidized state (Fraser and Parry, 2005). **C**. Keratin intermediate filaments are composed of seven tetramers that spiral longitudinally with one tetramer trapped internally. The lateral organization of the tetramers is slightly random (Er Rafik et al., 2004). Most head groups, and possibly tails may interact with the protein matrix in which filaments are embedded, with this interaction region having different chemo-physical properties than the rest of the matrix (Istrate et al., 2013) which is composed of keratin-associated proteins (KAPs). **Key**: Cons, consensus sequence; IF, keratin intermediate filament; L1 and L12 are linkers.

frames. Mounted samples were air dried before being placed in four changes of LR White acrylic resin (2 h × 2 and overnight on rotator) and polymerized for 19 h at 60 °C.

Sections cut (Ultracut UCT, Leica, Germany; 35° diamond knife, Diatome, Switzerland) at 100 nm onto copper grids with no support film were examined at 250 kV using a FEI (USA) Tecnai T3 TEM with Compustage to determine optimal sample thickness for tomography. 100 nm sections of Porcupine quill on 700 mesh hexagonal grids were selected. Comparison porcupine quill and wool cortex in some samples was made after section staining (uranyl acetate and lead citrate) using at 80 kV (FEI Morgagni 268D). Comparison of both of these samples were also made with Romney wool samples stained using 3 cycle reduction osmication as described in (Harland et al., 2011a).

For cryo-TEM and stain-free electron tomography, samples were coated at high vacuum with 2 nm carbon (Edwards E306A, Edwards High Vacuum, UK) and examined at 200 kV using a JEOL (Japan) JEM-2200FS Cryo-TEM with micrographs captured by a TVIPS-TemCam F416 (TVIPS-GmbH, Germany), and both controlled by Serial EM 3.4 software (University of Colorado, USA).

Tilt series were collected at 40,000× microscope magnification (pixel width 0.312 nm). For dry and hydrated samples both low-dose (focus on adjacent areas) and the energy filter were used to maximize the contrast and reduce sample degradation. Only transversely cut samples proved to reconstruct well enough to be used. Tomograms were reconstructed and examined using the IMOD 4.5.7 software suite (University of Colorado, USA).

For observation of hydrated sections using cryo-TEM, sections were placed on a 5 μL drop of distilled water for 10 min, removed, excess water wicked off with a filter paper and 15 nm gold fiducially applied in a 10% dilution droplet (5 μL) for 3 min. Excess liquid was wicked off and grid was immediately plunge frozen in liquid-nitrogen cooled ethane (Leica, KF80). Grids were stored under liquid nitrogen until examined.

Analysis of tomograms was carried out using IMOD and micrographs using AnalySIS Five (Olympus Imaging Systems, Germany). A mixture of image enhancement and spatial frequency tools were used to examine differences in low contrast images. Fast Fourier transforms were used to locate regions of micrographs and tomograms with high levels of structural spacing at around 8–11 nm, corresponding to the expected filament spacing. A few filaments were then located visually using virtual projections of full thickness (~80 nm) and by moving up and down through the tomogram using a virtual projection integrated from 16 to 30 slices. Many earlier electron microscopy and X-ray based studies have established that trichokeratin KIFs in their final state are close to 7.6 nm diameter. Likely boundaries of the filaments were determined by looking for circular patterns of this diameter. While many isolated filaments were found this way, further examination was given to the few regions where multiple circles were found in close proximity. Thresholding was then used to identify blobs of higher local electron density within and between the fitted 7.6 nm circles using single slices (0.31 nm thick). Further analysis was not possible due to the data quality and uncertainty over artifacts possibly caused by electron damage, the imaging and reconstruction process.

2.2. NMR

Merino wool fibers and genetically Caucasian origin (Western Europe, Brown, Eumelanin type) human scalp hair fibers. All fibers were cleaned by water washing and dried freely under controlled environmental conditions (55% relative humidity and 25 °C) before being used for further examinations. Proton solid state NMR spectra, ^{1}H double-quantum (DQ) build-up curves, ^{1}H spin diffusion, and ^{13}C CPMAS spectra were measured on a Bruker DSX-500 spectrometer operating at 500.45 and 125.84 MHz for ^{1}H and ^{13}C, respectively.

2.3. Transient electro-thermal (TET) technique

TET is a technique that measures the thermal diffusivity and thermal conductivity by inducing and detecting transient temperature change with an electrical current. In general, a step DC current is fed through the sample to introduce Joule heating and temperature rise. The electrical resistance of the sample will change and takes a while to reach the steady state. How fast/slow the resistance reaches the steady state is determined by the thermal diffusivity of the sample. The transient electrical resistance change can be reflected in the voltage change over the sample and is used for data fitting to determine the thermal diffusivity. More details about the technique could be found elsewhere (Guo et al., 2007; Liu et al., 2015). The TET technique has been used widely for measuring the thermal diffusivity of various fiber-like materials, including polymer, metal, and semiconductor. Samples were genetically Chinese (Han) origin scalp hair, previously only shampoo treated. The to-be-measured sample is suspended between two aluminum electrodes and placed in a vacuum chamber of a cryogenic system (CCS-450, JANIS), as shown in Fig. 2A. Samples are 1–1.5 mm in length and 60–100 um in width. Fig. 2B presents a hair sample suspended between two electrodes. The fiber–electrode contact is secured with silver paste to ensure excellent electrical and thermal contact. The vacuum level remains under 0.5 mTorr by a liquid nitrogen cold trapped mechanical vacuum pump to eliminate the effect of heat convection in the measurement.

During the thermal characterization, a square current offered by a current source (Keithley 6221) is fed through the fiber to induce Joule heating. The temperature rise caused by the Joule heating will lead to a rise of the sample resistance and thus the voltage over the fiber. An oscilloscope (Tektronix DPO3052) is used to monitor the voltage evolution over the fiber. How fast/slow the vol tage/resistance/temperature increases with time to reach the steady state is determined by the thermal diffusivity of the sample and its length. A physical model has been developed to fit the transient voltage variation to determine the sample's thermal diffusivity. (Guo et al., 2007) The model is introduced in detail together with experimental data in the result section. In the measurement, since hair is not electrically conductive, a very thin metallic coating (iridium, Ir, film of ~nm thickness) is sputter coated on the hair to make it electrically conductive. The effect of the Ir coating on the measurement results can be well subtracted based on the Wiedemann-Franz law. The thermal radiation effect hair's surface is also considered with high accuracy as described later in this paper.

3. Results and discussions

3.1. Results of TEM analysis

Transversely sectioned porcupine quill cortex which was section stained with lead and uranium salts showed a similar subcellular morphology to that of wool, human scalp hair and other mammalian hairs. Keratin was clearly arranged in cohesive macrofibrils surrounded by cytoplasmic remnant material with cortex cells joined by a cell membrane complex (Fig. 3A). Section staining revealed intermediate filaments within macrofibrils that tended to be tightly hexagonally packed (Fig. 3B). Macrofibril architecture was nematic (lattice-like unidirectional packing), making them something like mesocortex-packed paracortex observed in wool (Harland et al., 2011b; Thomas et al., 2012).

Contrast was unsurprisingly low in the dry and hydrated unstained porcupine samples (Fig. 3C), but at lower magnification some features such as the edge of cortex cells were occasionally visible due to their lower electron density. Beam damage artifacts were seen in the hydrated sample with relatively little beam exposure required to cause bubbling (Fig. 3C). The bubbling phenomenon appeared similar to that described for electron beam effects on dried sodium phosphate buffer (Massover, 2010). In some locations increased beam exposure led to bubbles enlarging and merging until the sample under the beam was clear of the artifact, or baked out. Keratin intermediate filaments were not clearly identified using TEM in dry (Fig. 3D) or baked out hydrated sample (Fig. 3E). However, analysis by Fast-Fourier Transform indicated a difference between the samples in some feature at 7 nm spacing in the dry sample and a similar signal at 9 nm spacing in the wet sample. Given the lack of clarity in the images and the artifacts, we don't feel confident assigning this 2 nm change to a particular feature.

The blobs and variable pattern that appears within transversely cut KIFs of conventionally stained wool cortex (Fig. 3G) has been considered a kind of phase contrast artifact caused by electron diffraction due to the tube-like morphology of the filament (Millward, 1970), and it was concluded that KIFs are laterally symmetrical and uniform in terms of the organization of their constituent protofibrils. This view of lateral symmetry disagrees with recent work with micro-beam synchrotron results which suggest some lateral disorder in protofilament arrangement within KIFs (Er Rafik et al., 2004). The grainy appearance of the KIF and its surrounding matrix could also be attributed to chemical staining artifacts (Fraser et al., 2003). Electron tomography of unstained material goes some way to control for both artifact types at the

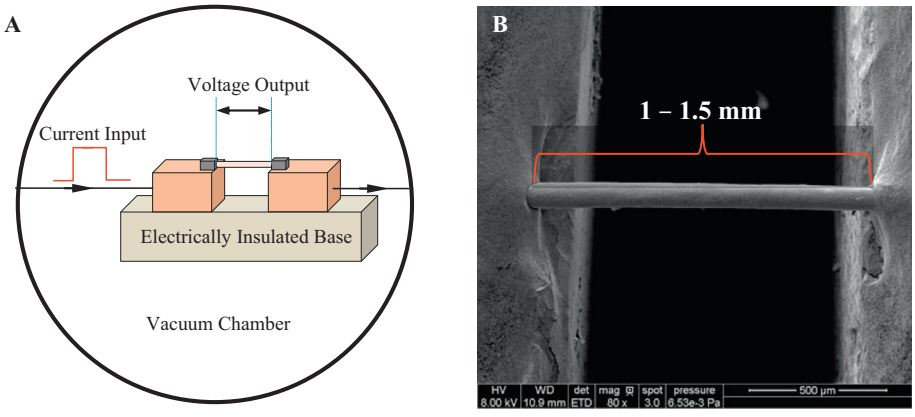

Fig. 2. TET measurement for human hair. (Xu, 2015). **A.** Experimental set-up for TET measurement. The aluminum electrodes are insulated from the aluminum base by thin mica layers. The electrodes are connected to a DC current source and an oscilloscope. The base is attached to the cold head of cryogenic system by vacuum grease. Human hair sample is coated with 20 nm iridium layer to be electrically conductive. **B.** SEM image of a prepared human hair sample.

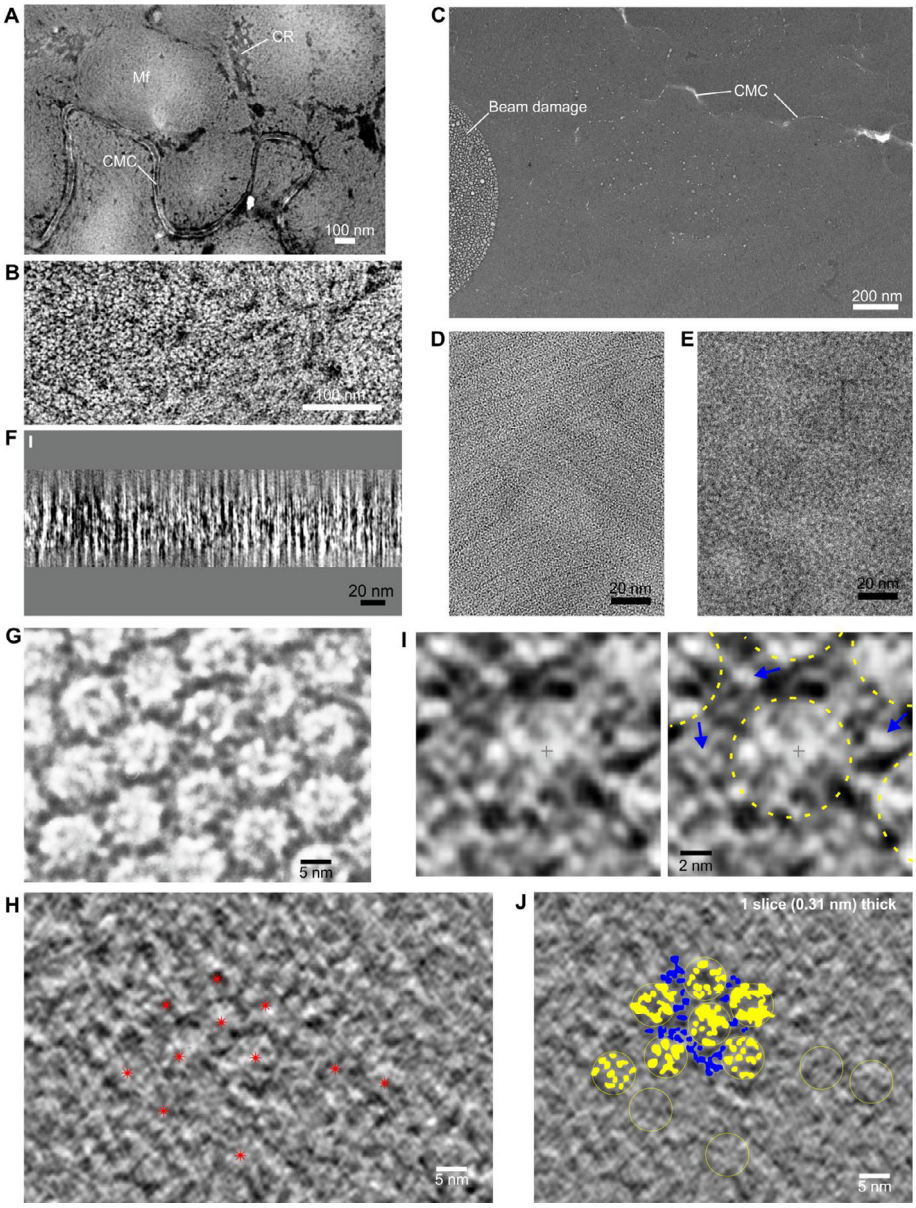

Fig. 3. Electron microscopy of fiber cortex. **A**. Grid stained low magnification micrograph of the cortex of *Hystrix cristata* quill illustrating typical cortical features (CMC, cell membrane complex; CR, cytoplasmic remnant; Mf, macrofibril). **B**. Grid stained *H. cristata* cortex showing KIFs in matrix. **C**. Cryo-TEM micrograph of *H. cristata* cortex illustrating CMC and beam damage. **D** and **E** are high magnification micrographs of *H. cristata* cortex in dry and hydrated sections respectively. **F**. Virtual longitudinal projection through electron tomogram of dry *H. cristata* cortex illustrating filaments. **G**. Transverse section of conventionally stained Romney wool cortex showing slightly random lateral appearance of KIFs and blobs between KIFs. **H**. A 5 nm thick (16 slice) virtual projection of a central part of a tomogram of unstained *H. cristata* cortex. Presumed KIFs are indicated with red stars. **I**. Blown up region of a single slice (0.31 nm) illustrating KIF extent with dashed yellow line and examples of some interfilament grains (blue arrows). **J.** Single slice of projection in panel H, with circles around edges of some KIFs and density map drawn of the KIFs (yellow) and matrix (blue).

expense of image contrast because only protein is available to block the electron beam and the image examined comes from within a tomogram reconstructed from dozens of individual projections of the same KIF taken from a wide range of angles. The electron-tomography of dry un-stained porcupine cortex produced results where it was possible to identify patches of individual KIFs in longitudinal (Fig. 3F) and transverse section (Fig. 3H). In some cases, it was possible to visualize structure within and around KIFs in individual slices (0.3 nm thick) or a few slices combined (e.g., 1–5 nm thick) (Fig. 3I). The results clearly suggested that filament and surrounding matrix are different in terms of protein organization and that both have a heterogeneous organization with the matrix being composed of dense grains surrounded by low density areas (Fig. 3J). Further characterization of the structures to provide sizes or shapes was not possible with the quality of images here.

3.2. Results of solid-state ^{1}H NMR analysis

We used magic angle spin solid-state NMR (MAS SSNMR) spectroscopy for evaluating the phase composition of keratin fibers (Melian et al., 2009). The signal of solid-state ^{1}H NMR obtained for various keratin fibers (wool and human hair, respectively) was deconvoluted into three phases, namely rigid, mobile and interface, following the 3-phase model for keratin materials (Istrate et al., 2013): crystalline, amorphous and interface, and the material composition was thus calculated. Comparing the amount of rigid phase calculated this way with those reported in

literature for XRD evaluated crystallinity of keratin fibers we notice a significantly large difference: 60...75% rigid phase by NMR (Melian et al., 2009) versus 21–35% crystallinity by XRD (Spei and Holzem, 1989). The more than double amount of rigid phase obtained from NMR measurements suggests that it reflects not only the defined crystalline structures provided by XRD experiments which are consider to be the KIFs assembles, but some other ordered structures of smaller size than those of the microfilaments.

Using the spin diffusion theory as proposed in the literature (Clauss et al., 1993) the dimensions of the particles of the rigid phase were shown to be independent on the morphology (for a square, or a cylindrical morphology) and related to the spin diffusion time, t_d (Baias et al., 2009a):

$$d_R \sim \frac{\sqrt{D_R D_M}}{\frac{\rho_R}{\rho_M}\sqrt{D_R}+\sqrt{D_M}} t_d^{1/2} \tag{1}$$

where $\rho_{R,M}$ are the numbers density spin in "rigid" and in "mobile" phase respectively, and $D_{R,M}$ are the spin diffusion coefficients in "rigid" and "mobile" phase respectively.

Values calculated for the sizes of the constituents of the rigid phase from spin diffusion experiments run on human hair untreated, bleached and perm-waved, respectively, are listed in Table 1 below, as taken from reference (Baias et al., 2009b).

Compared with the KIFs size, the dimensions calculated for the rigid domain particles at 3–5 nm (see Table 1) are, by far (10 times), smaller than those of the crystalline KIF domain at 47 nm (comparable with only segments 1A and 2A of the alpha-helical rods (Steinert et al., 1993). This suggests that the rigid domain, which is more than doubled the amount of crystalline domain, is made of a significant quantity of small ordered components of a size below 5 nm at room temperature.

NMR experiments indicate that the size of rigid domains is dependent on chemical treatments of the keratin material (see Table 1), by increasing at oxidation and decreasing at perm-waving, apparently being sensitive to the status of disulfide bonds. Since these bonds are not part of the KIFs, being found only in low amounts in the linkers and in the tails of alpha-helical rods (Spei and Holzem, 1989), but they exist mainly in the matrix, we tend to believe that the rigid domains identified by solid-state ^{1}H NMR describe components of the matrix along with those of crystalline filaments.

3.3. Results of TET analysis

Single hair fibers were measured for their thermal conductivity by the help of Transient Electro-Thermal Technique (TET), which has been described elsewhere, together with the measuring device developed for performing the measurements of thermal diffusivity at controlled temperatures (Guo et al., 2007).

The heat is conducted through the insulator keratin material by phonons. Their diffusion is governed by the well-known equation (Liu et al., 2015):

$$\frac{\partial T}{\partial t} = \frac{\kappa}{\rho c_p}\frac{\partial^2 T}{\partial x^2} + \dot{q}, \tag{2}$$

Table 1
Rigid domain sizes for untreated and cosmetically treated human hair at 25 °C, 55% relative humidity.

Sample	Dimension of rigid domain particles, d_R/nm
Caucasian human hair	4.5
Caucasian human hair bleached 3×	5.5
Caucasian human hair perm-waved 3×	3.0

where κ is the thermal conductivity, c_p is the specific heat of the keratin material and ρ is its density, $\dot{q}$ being the heat generation in the sample during TET measurement. The ratio $\kappa/(\rho\ c_p) = \alpha$ is the thermal diffusivity of the material and its value helps characterizing the domain size through which the phonons travel, according to the following dependence:

$$Domain\ size \sim \left(\frac{\kappa}{\rho c_p}\cdot t_d\right)^{1/2} \tag{3}$$

where t_d is the time of phonon diffusion.

For finding the value of the thermal diffusivity for keratin fiber one needs to consider that the value of effective thermal diffusivity, α_{eff}, as obtained from fitting the experimental curve with the theoretical solution of a 1-D heat transfer equation (see Fig. 4):

$$T^*(t) = \frac{96}{\pi^4}\sum_{m=1}^{\infty}\frac{1-\exp[-(2m-1)^2\pi^2\alpha_{eff}t/L^2]}{(2m-1)^4} \tag{4}$$

where L is the length of keratin fiber used in experiment, is composed of a contribution of the thermal diffusivity of Iridium, $\alpha_{Iridium}$, used for coating the fiber:

$$\alpha_{Iridium} = \frac{Lo_{Iridium}TL^2}{RV\rho c_p} \tag{5}$$

with $Lo_{Iridium}$ being the Lorenz number, R being the electrical resistance of Iridium and V is the volume of keratin fiber, and a contribution of heat lost by radiation, $\alpha_{radiation}$:

$$\alpha_{radiation} = \frac{8\varepsilon_r\sigma T_0^3 L^{\frac{5}{2}}}{\pi^{\frac{3}{2}}\rho c_p V^{\frac{1}{2}}} \tag{6}$$

where σ is Stefan-Boltzmann constant and ε_r is the effective emissivity of the sample.

The value of keratin thermal diffusivity, $\alpha_{keratin}$, is finally determined as

$$\alpha_{Keratin} \approx \alpha_{eff} - \alpha_{Iridium} - \alpha_{radiation} \tag{7}$$

This way we determined the values of various fibers obtained from hair samples provided by different people. The results, listed in Table 2, indicate that the values of thermal diffusivity increase

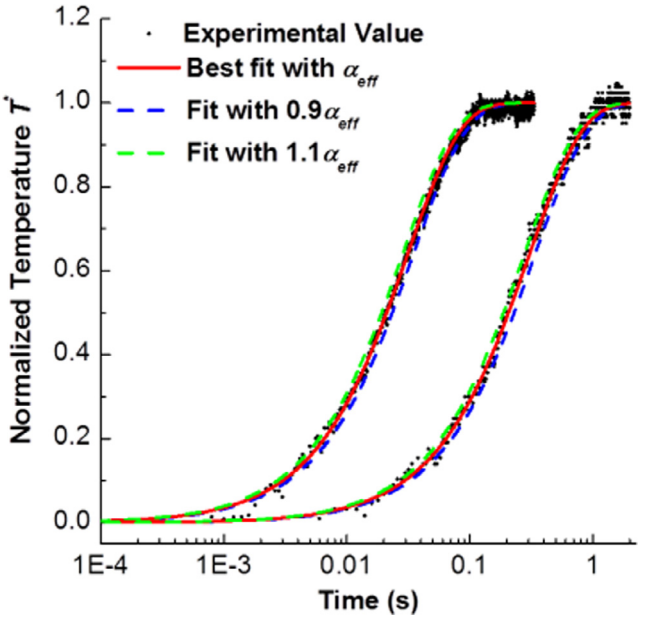

Fig. 4. Obtaining the value of effective thermal conductivity, α_{eff}, by fitting experimental data with the theoretical solution (Eq. (4)).

Table 2
Thermal diffusivity of hairs sourced from different people. Hair snippets were taken from the root of the fiber (material close to scalp) for ensuring material less affected by environmental factors.

Age/(Years)	4	25	27	29	30	62
Thermal Diffusivity, $\alpha/(\times 10^{-7}\ m^2\ s^{-1})$	1.01	1.24	1.42	1.41	1.53	1.49

with age until about 25–26 years old, after which they plateau at around $(1.4–1.5) \times 10^{-7}\ m^2 s^{-1}$.

Using a cryogenic arrangement we were able to examine the effect of temperature on the values of thermal diffusivity, α, by running measurements on the same fiber for temperature ranging from around 300 K down to 10 K. A group of results is graphed in Fig. 5. Note that the effective thermal conductivity is derived from $\kappa_{eff} = I^2RL/(12\Delta TA)$, where ΔT is temperature rise during a single step and specific heat is evaluated by $\rho c_p \approx \kappa_{eff}/\alpha_{eff}$. The keratin thermal conductivity is determined as $\kappa = \alpha_{Keratin}\rho c_p$.

Defining thermal reffusivity, Θ, as the reverse of thermal diffusivity:

$$\Theta = 1/\alpha_{Keratin} \tag{8}$$

we were able to plot the evolution of this new variable with temperature, as in Fig. 6.

One observes in Fig. 6b that, extrapolating to 0 K the residual thermal reffusivity, Θ_0, of the perfect crystal it becomes nil, while for keratin material it has a defined value, namely $2.1 \times 10^6\ s\ m^{-2}$.

The variation of thermal reffusivity with temperature, as in Fig. 6, indicates a definite structure of the material through which the phonon diffuses. The physical model for phonon interaction with keratin as an insulator is illustrated in Fig. 7. Accordingly, one may write for thermal reffusivity:

$$\Theta = \frac{1}{\alpha} = \frac{3}{v^2 \cdot \tau} = \frac{3}{v}\left(\frac{1}{l_{ph-ph}} + \frac{1}{l_{def}}\right) \tag{9}$$

where v is the phonon velocity, τ is the phonon relaxation time, $\tau^{-1} = \tau_{ph-ph}^{-1} + \tau_{def}^{-1}$, and $l = v\,\tau$ is the phonon mean free path (Liu et al., 2015). This single relaxation time approximation can be more precisely refined if the phonon's density of state is given, as detailed in our work (Guo et al., 2007). Without knowing the exact phonon dispersion relation and density of state, Eq. (9) still provides sound evaluation of the structure domain size due to phonon diffusion.

In Eq. (9) the first term in bracket becomes zero for temperature tending to 0 K (as $l_{ph\text{-}ph} \rightarrow$ infinity). As a consequence, for T → 0 the residual thermal reffusivity, Θ_0, equals:

$$\Theta_0 = 1/\alpha = 3/(v l_{def}) \tag{10}$$

Eq. (10) provides the way to evaluate the domain size, l_{def}, from residual thermal reffusivity. The exact value of phonon velocity in keratins, v, is unknown so far; for the purpose of the present paper we used the value of 1000 m s^{-1}, reported in other experiments with phonons in proteins (Achterhold and Parak, 2003). From the residual thermal reffusivity as calculated from Fig. 6A, of $2.1 \times 10^6\ s\ m^{-2}$, and the assumed value of phonon velocity in proteins of 1000 m s^{-1} one may calculate a domain size for keratin in a sample of virgin human hair of:

$$Domain\ size \approx l_{def} \approx 1.43\ nm$$

Following this methodology the values of domain size for treated hair fibers were also inferred and listed in Table 3.

Taken together, the TET, NMR and electron tomography results suggest that the inter-KIF matrix of hair is composed of tight grains, with some degree of regular organization and in the range of 2–4 nanometres in diameter. Our argument for this conclusion is as follows:

1. The closeness of the domain size values from Table 1 with those from Table 3, despite different physical parameters being measured and a 300 degrees difference between the temperatures at which the measurements were performed, suggests a nano-scale structure within samples that has a grain size of 2–4 nm.
2. The measured grains were readily affected by chemical processing that does not affect KIFs (Fraser et al., 1964).
3. The size range of 2–4 nm is compatible with the approximate size of many keratin associated proteins.
4. Electron tomography data observations also suggest a grain component of the matrix.

The proposed nano-scale grainy structure of the matrix seems to be further endorsed by results from TET measurements of white and brown hair fibers from same source (a ponytail of grey hair) which found that the thermal diffusivity of white hairs is higher with some 40–50% than those of brown hairs ($2.43 \times 10^{-7}\ m^2\ s^{-1}$

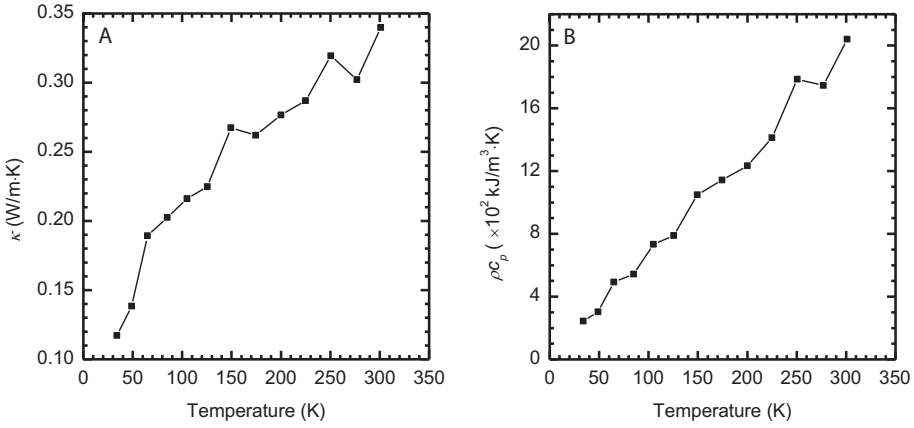

Fig. 5. Thermal characterization for temperature ranging from ~300 to 10 K. **A.** evolution of thermal conductivity, **κ**, with temperature; **B.** change of specific heat, ρc_p, with temperature.

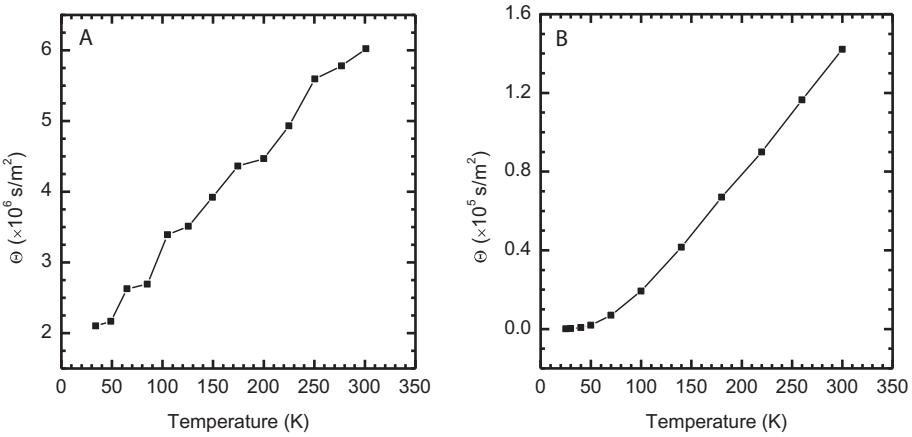

Fig. 6. Evolution of thermal reffusivity with temperature going down to 10 K for a hair fiber (**A**) and for a perfect crystal, as of NaF (**B**).

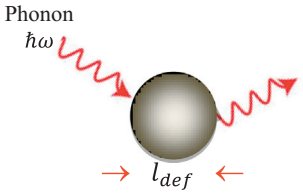

Fig. 7. The pathway of phonon through the insulator.

Table 3
Mean domain size from TET measurements.

Samples	$\Theta_0/(\times 10^6\ s\ m^{-2})$	Domain size/(nm)
Caucasian human hair	2.46	1.22
Caucasian human hair bleached 3x	1.52	1.97
Caucasian human hair perm-waved 3x	1.71	1.75

versus $1.72 \times 10^{-7}\ m^2\ s^{-1}$) as recorded under same temperature (300 K). Even more striking, TET measurement of hair fibers sampled from people diagnosed with breast cancer and before beginning of any treatment records values of thermal diffusivity of doubled the value measured for hair from healthy people ($2.96–3.51 \times 10^{-7}\ m^2\ s^{-1}$ compared with $1.53–1.72 \times 10^{-7}\ m^2\ s^{-1}$). We consider that at this stage it is quite speculative to interpret these results beyond being a hint for the nano-scale structure of the matrix which changes when melanin is no more produced, or when early breast disorders affect probably the hair production in follicles. It is, nevertheless, a field deserving further investigations for the potential usage of the method as marker, for example.

The grainy nano-scale structure of matrix suggested by this work appears to be in line with the presence of the globular KAPs proteins in the matrix as in some models proposed for explaining the stress-strain properties of wool by Crewther (Crewther, 1965), or Feughelman (Feughelman, 1994), and critically summarized by Hearle (Hearle, 2000). The theoretically estimated linear dimension of KAPs at 3 nm (Naito et al., 1996; Hearle, 2000), matches also the present data. Graphically, the model of matrix supported by our results is similar to the 'beaded' model of Crewther (Crewther, 1965). Our study goes further, still, indicating that these grains possess a certain order at the nano-scale, as requested by the phonon behavior in TET measurements, which implies a nano-scale organization of proteins and not a random packing of chains, densely cross-linked by disulfide bonds.

4. Conclusions

Using three largely different tools for investigating keratin fibers, namely TEM, solid-state NMR and Transient Electro-Thermal Technique, TET, we suggest that the matrix of keratin fiber cortex, far from being amorphous, has a grainy structure. The results from measuring the spin diffusion and thermal reffusivity on hair fibers indicate the size of these grains to be around 2–4 nm, strongly depending on the chemical treatment of the fiber, on the temperature and on the relative humidity of the environment, as well as on the physiological factors at the level of fiber production in follicle.

The fact that the matrix has a nano-scale structure leads to further questions concerning the function and the purpose of this structure, which are, however, beyond the scope of the present work.

Author contributions

C.P., X.W., D.H. and M.K. envisioned and designed research; C.P., X.W., B.Z., J.L., D.H. and M.K. performed research; X.W. developed the TET technique; C.P., X.W., D.H. and M. K. analyzed data and wrote the paper.

Acknowledgements

We gratefully acknowledge the assistance of Richard Easingwood and Sharon Lequeux from the Otago Centre for Electron Microscopy for assistance with collecting cryo-TEM and tomography data, and James Vernon for TEM sample preparation. Partial funding (DPH) for this project was provided by the Wool Consortium (Contract number: A18223) and AgResearch Core Funding (ex-FRST/MBIE C10X0710).

References

Achterhold, K., Parak, F.G., 2003. Protein dynamics: determination of anisotropic vibrations at the haem iron of myoglobin. J. Phys. Condens. Mater. 15 (18), S1683–S1692.
Baias, M., Demco, D.E., Popescu, C., Fechete, R., Melian, C., Bluemich, B., Moeller, M., 2009a. Thermal denaturation of hydrated wool keratin by 1H solid-state NMR. J. Phys. Chem. B 113, 2184–2192.
Baias, M., Demco, D.E., Istrate, D., Popescu, C., Bluemich, B., Moeller, M., 2009b. Morphology and molecular mobility of fibrous hard alpha-keratins by 1H, 13C, and 129Xe NMR. J. Phys. Chem. B 113, 12136–12147.
Chernyatina, A.A., Guzenko, D., Strelkov, S.V., 2015. Intermediate filament structure: the bottom-up approach. Curr. Opin. Cell. Biol. 32, 65–72.
Clauss, J., Schmidt-Rohr, K., Spiess, H.W., 1993. Determination of domain sizes in heterogeneous polymers by solid-state NMR. Acta Polym. 44, 1–17.
Crewther, W.G., 1965. The stress-strain characteristics of animal fibres after reduction and alkylation. Textile Res. J. 35, 867–877.

Er Rafik, M., Doucet, J., Briki, F., 2004. The intermediate filament architecture as determined by X-ray diffraction modeling of hard α-keratin. Biophys. J. 86, 3893–3904.
Feughelman, M., 1994. A model for the mechanical properties of the alpha-keratin cortex. Textile Res. J. 64, 236–239.
Fraser, R.D.B., MacRae, T.P., Miller, A., 1964. The coiled-coil model of alpha-keratin structure. J. Mol. Biol. 10, 147–156.
Fraser, R.D.B., Steinert, P.M., Parry, D.A.D., 2003. Structural changes in trichocyte keratin intermediate filaments during keratinization. J. Struct. Biol. 142 (2), 266–271.
Fraser, R.D.B., Parry, D.A.D., 2005. The three-dimensional structure of trichocyte (hard α-) keratin intermediate filaments: features of the molecular packing deduced from the sites of induced crosslinks. J. Struct. Biol. 151 (2), 171–181.
Guo, J., Wang, X., Wang, T., 2007. Thermal characterization of microscale conductive and nonconductive wires using transient electrothermal technique. J. App. Phys. 101, 063537.
Harland, D.P., Caldwell, J.P., Woods, J.L., Walls, R.J., Bryson, W.G., 2011a. Arrangement of trichokeratin intermediate filaments and matrix in the cortex of merino wool. J. Struct. Biol. 173, 29–37.
Harland, D.P., Vernon, J.A., Walls, R.J., Woods, J.L., 2011b. Transmission electron microscopy staining methods for the cortex of human hair: a modified osmium method and comparison with other stains. J. Microsc. 243 (2), 184–196.
Hearle, J.W.S., 2000. A critical review of the structural mechanics of wool and hair fibres. Int. J. Biol. Macromol. 27, 123–138.
Istrate, D., Popescu, C., Er Rafik, M., Moeller, M., 2013. The effect of pH on the thermal stability of fibrous hard alpha-keratins. Polymer Degrad. Stab. 98, 542–549.
Liu, J., Xu, Z., Cheng, Z., Xu, S., Wang, X., 2015. Thermal conductivity of ultra-high molecular weight polyethylene crystal: defect-effect uncovered by 0 K limit phonon diffusion. ACS Appl. Mater. Interfaces 7 (49), 27279–27288.
Lynch, M.H., O'Guin, W.M., Hardy, C., Mak, L., Sun, T.T., 1986. Acidic and basic hair/nail ('hard') keratins: their colocalization in upper cortical and cuticle cells of the human hair follicle and their relationship to 'soft' keratins. J. Cell Biol. 103, 2593–2606.
Massover, W.H., 2010. Electron beam-induced radiation damage: the bubbling response in amorphous dried sodium phosphate buffer. Microsc. Microanal. 16, 346–357.
Melian, C., Demco, D.E., Istrate, M., Balaceanu, A., Moldovan, D., Fechete, R., Popescu, C., Moeller, M., 2009. Morphology and side-chain dynamics in hydrated hard alpha-keratin fibres by 1H solid-state NMR. Chem. Phys. Lett. 480, 300–304.
Millward, G.R., 1970. The substance of alpha-keratin microfibrils. J. Ultrastruct. Res. 31, 349–355.
Naito, S., Arai, K., Hirano, M., Nagasawa, N., Sakamoto, M., 1996. Crosslinking structure of keratin. V. Number and type of crosslinks in microstructures of untreated and potassium cyanide treated human hair. J. Appl. Polym. Sci. 61 (11), 1913–1925.
Parry, D.A.D., 2006. Hendecad repeat in segment 2A and linker L2 of intermediate filament chains implies the possibility of a right-handed coiled-coil structure. J. Struct. Biol. 155, 370–374.
Parry, D. A. D., Fraser, R. D. B., 2015. Personal communication.
Popescu, C., Hoecker, H., 2007. Hair—the most sophisticated biological composite material. Chem. Soc. Rev. 36, 1282–1291.
Schrooyen, P.M.M., Dijkstra, P.J., Oberthür, R.C., Bantjes, A., Feijen, J., 2000. Partially carboxymethylated feather keratins. 2. Thermal and mechanical properties of films. J. Agric. Food Chem. 48 (9), 4326–4334.
Smith, T.A., Strelkov, S.V., Burkhard, P., Aebi, U., Parry, D.A.D., 2002. Sequence comparisons of intermediate filament chains: Evidence of a unique functional/structural role for coiled-coil segment 1A and linker L1. J. Struct. Biol. 137, 128–145.
Spei, M., Holzem, R., 1989. Thermoanalytical determination of the relative helix content of keratins. Colloid Polym. Sci. 267, 549–551.
Steinert, P.M., Marekov, L.N., Fraser, R.D.B., Parry, D.A.D., 1993. Keratin intermediate filament structure. J. Mol. Biol. 230, 436–452.
Thomas, A., Harland, D.P., Clerens, S., Deb-Choudhury, S., Vernon, J.A., Krsinic, G.K., Walls, R.J., Cornellison, C.D., Plowman, J.E., Dyer, J.M., 2012. Interspecies comparison of morphology, ultrastructure and proteome of mammalian keratin fibres of similar diameter. J. Agric. Food Chem. 60, 2434–2446.
Trabbic, K.A., Yager, P., 1998. Comparative structural characterization of naturally and synthetically-spun fibers of Bombyx mori fibroin. Macromolecules 31 (2), 462–471.
Wang, B., Yang, W., McKittrick, J., Meyers, M.A., 2016. Keratin: Structure, mechanical properties, occurrence in biological organisms, and efforts at bioinspiration. Prog. Mater. Sci. 76, 229–318.
Xu, Z., 2015. Thermal Transport in DNA. Iowa State University. Graduate Theses and Dissertations. 14727.
Zhao, C., Yao, J., Masuda, H., Kishore, R., Asakura, T., 2003. Structural characterization and artificial fiber formation of *Bombyx mori* silk fibroin in hexafluoro-iso-propanol solvent system. Biopolymers 69 (2), 253–259.